Marine Structures 79 (2021) 103047

Contents lists available at ScienceDirect

# Marine Structures

journal homepage: www.elsevier.com/locate/marstruc

# LQR control on multimode vortex-induced vibration of flexible riser undergoing shear flow

Jixiang Song [a,b], Weimin Chen [a,b,*], Shuangxi Guo [a,b], Dingbang Yan [a,b]

[a] Key Laboratory for Mechanics in Fluid-Solid Coupling Systems, Institute of Mechanics, Chinese Academy of Sciences, Beijing, 100190, China
[b] School of Engineering Sciences, University of Chinese Academy of Sciences, Beijing, 100049, China

ARTICLE INFO

*Keywords:*
Flexible riser
Vortex-induced vibration
Active control
LQR method

ABSTRACT

Under the actions of ocean currents and/or waves, deep-sea flexible risers are often subject to vortex-induced vibration (VIV). The VIV can lead to severe fatigue and structural safety issues caused by oscillatory periodic stress and large-amplitude displacement. As flexible risers have natural modes with lower frequency and higher density, a multimode VIV is likely to occur in risers under the action of ocean currents, which is considered as shear flow. To decrease the response level of the VIV of the riser actively, a multimode control approach that uses a bending moment at the top end of the riser via an LQR optimal controller is developed in this study. The dynamic equations of a flexible riser including the control bending moment in shear flow are established both in the time and state-space domains. The LQR controllers are then designed to optimize the objective function, which indicates the minimum cost of the riser's VIV response and control input energy based on the Riccati equation of the closed-loop system under the assumption that the lift coefficient distribution is constant. Finally, the VIV responses of both the original and closed-loop systems under different flow velocities are examined through numerical simulations. The results demonstrate that the designed active control approaches can effectively reduce the riser displacement/angle by approximately 71%–89% compared with that of the original system. Further, for multimode control, the presented mode-weighted control is more effective than the mode-averaged control; the decrease in displacement is approximately 1.13 times than that of the mode-averaged control. Owing to the increase in flow velocity as more and higher-order modes are excited, the VIV response of the original system decreases slightly while the frequency response gradually increases. For the closed-loop system, the response becomes smaller and more complicated, and the efficiency of the controller becomes lower at a certain flow velocity.

## 1. Introduction

With increasing sea depth, riser flexibility and response amplitude can increase significantly. These large-amplitude responses of the marine riser including the forced and random vibrations, vortex-indued vibration (VIV), collapse, and buckling, can further decrease the structural fatigue life and endanger the entire deep-sea oil and gas acquisition system. To avoid these issues, it is necessary to focus on riser vibration control in the design of the riser structure.

* Corresponding author. Key Laboratory for Mechanics in Fluid-Solid Coupling Systems, Institute of Mechanics, Chinese Academy of Sciences, Beijing, 100190, China.
*E-mail address:* wmchen@imech.ac.cn (W. Chen).

https://doi.org/10.1016/j.marstruc.2021.103047
Received 14 June 2020; Received in revised form 5 April 2021; Accepted 14 June 2021
Available online 21 June 2021
0951-8339/

Riser vibration control includes passive control, which does not require input power, and active control, which requires input power [1,2]. Passive control devices include helical strakes, O-rings, fairings, axial rods, ribbons, etc. [3–5]. Because passive control is easier to manufacture and implement, it is used widely in offshore engineering applications [6,7]; further, helical strakes are the most widely used [8,9] because they reduce the VIV response by breaking regular vortex shedding along the flow direction and preventing coincident shedding perpendicular to the flow direction, thereby suppressing the overall response of the riser. However, the inevitable presence and moderate amounts of marine growth quickly negate any suppression caused by the strakes [10]. Further, suppressing the local response is often important. The top riser angle is limited when the riser is in service [11]. The boundary control not only reduces the top corner of the riser but also reduces the vibration displacement and stress amplitude of the riser; therefore, the boundary control in the active control has received widespread attention.

Do and Pan [12] designed a boundary controller based on Lyapunov's direct method and backstepping technology. Then, they changed the two-dimensional boundary control to three-dimensional boundary control [13]. How and Ge [11] applied the boundary control method to marine risers. The torque actuator controlled by Lyapunov is applied to the top of the riser, and the measurements required for feedback are the included angle at the top of the riser and the rate of change of the included angle. Ge and He [14] designed two actuators based on the Lyapunov direct method in both the horizontal and vertical directions. The control device is applied to the top boundary of the riser to minimize the vibration of the riser. Nguyen and Do [15] used the Lyapunov direct method to design the boundary controller in a two-dimensional environment. He and Zhang [16] developed an adaptive control method to control the marine riser installation system based on Lyapunov's direct method. Further, Zhang and He [17] installed three actuators on top of the riser. The boundary control method was based on the integral-barrier Lyapunov function. The numerical analysis results indicate that under time-varying disturbances, the designed control device can suppress the vibration of the riser and ensure that the joint angles are within the constrained ranges. Further, Zhao and Liu [18] used the Lyapunov theory and backstepping method as done in the study by Do and Pan [12]; however, they introduced new functions: a smooth hyperbolic tangent function, an auxiliary system, and a Nussbaum function. This method can effectively solve input saturation and external interference; however, the choice of the Lyapunov function is empirical, arbitrary, and not unique, which determines whether the control is successful. In addition, it is often difficult to obtain the optimal Lyapunov function.

In addition to the Lyapunov method, there are many methods for boundary control in the active control of the riser vibration. Shaharuddin and Darus [19] developed an auto-tuned PID controller algorithm implemented for suppressing the riser vibration. Further, the PID active vibration controller (PID-AVC) was developed using the iterative learning algorithm (ILA) within the MATLAB Simulink environment. The PID-AVC suppressed the VIV. Zhang and Li [20] proposed the use of a linear quadratic Gaussian controller to control the axial dynamic stress response of deep-water risers actively. They used a winch to reduce the axial dynamic stress response of deep-water risers, and the numerical analysis showed that the method was effective. Recently, Yu and Chen [21] set a torque actuator on the upper boundary of the riser and designed the control law based on the linear quadratic regulator (LQR) method. Their numerical simulations of the responses of the open-loop and closed-loop systems proved that this active control method is effective. Previous studies on the active control of marine riser vibration focused on overall vibration suppression, and not specifically on VIV vibration. The VIV of the riser is a major concern related to the fatigue and damage of the riser [8,22]. In addition, uniform flow and/or a simple sinusoidal hydrodynamic force were considered in the active control of riser vibration in most studies. However, in practice, the ocean current profile is nonuniform, and it is more similar to shear flow. Therefore, in this paper, a boundary control approach is developed based on the LQR method considering a shear flow.

The main contributions of this paper are as follows: an LQR optimal controller considering multimode VIV is designed, and the responses of the closed-loop systems using mode-weighted and mode-averaged approaches are analyzed and compared. Further, the effect of the shear flow velocities on the closed-loop system response are studied.

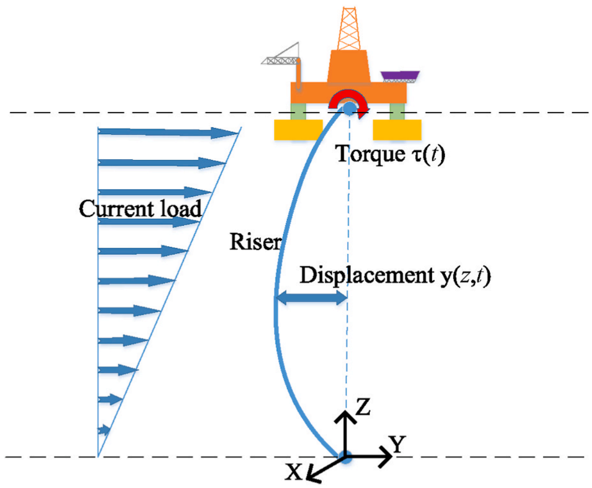


**Fig. 1.** Schematic of marine riser.

The remainder of this paper is structured as follows. In Section 2, the riser's dynamic equations with the controlling input torque are developed, and a proposed lift coefficient for VIV is used to predict the VIV of the riser in the frequency domain. In Section 3, the control law design based on LQR is applied to suppress multimode VIV. Our numerical results and discussions are presented in Section 4. The influences of the shear flow velocities on the closed-loop system response are examined. The conclusions drawn are presented in Section 5.

## 2. Analysis methodology and numerical models

### 2.1. Dynamics of marine riser

The reference frame for the riser is shown in Fig. 1. The governing differential equation of the riser dynamics is [11].

$$EI\frac{\partial^4 y(z,t)}{\partial z^4} - T\frac{\partial^2 y(z,t)}{\partial z^2} + m_z\frac{\partial^2 y(z,t)}{\partial t^2} + c\frac{\partial y(z,t)}{\partial t} - f(z,t) = 0 \tag{1}$$

where $y$, $z$, $t$, $EI$, $T$, $m_z$, $c$, and $f(z,t)$ denote the transverse displacement of the riser, length position, time, bending stiffness, tension, uniform mass per unit length of the riser, damping coefficient per unit length including structural damping and hydrodynamic damping, and transverse force per unit length, respectively.

The boundary conditions are

$$y(0,t) = 0 \tag{2}$$

$$EI\frac{\partial^2 y(0,t)}{\partial z^2} = 0 \tag{3}$$

$$y(L,t) = 0 \tag{4}$$

$$EI\frac{\partial^2 y(L,t)}{\partial z^2} - \tau(t) = 0 \tag{5}$$

The ocean current acts on the three-dimensional riser, and the external load generated is divided into the in-line drag force $F_D(z,t)$ and the oscillating lift $F_L(z,t)$ [23,24].

$F_L(z,t)$ is expressed as

$$F_L(z,t) = \frac{1}{2}\rho C_L\left(\frac{A}{D}\right)U^2(z)D\cos(2\pi f_v t + \phi) \tag{6}$$

where $C_L(A/D)$, $A$, $D$, $\rho$, $U$ (z), and $\phi$ denote the spatially varying lift coefficient, displacement, diameter of riser, sea water density, velocity of the current, and phase angle, respectively. Further, $f_v$ denotes the nondimensional vortex shedding frequency expressed as

$$f_v = \frac{S_t U}{D} \tag{7}$$

where $S_t$ denotes the Strouhal number; it usually takes the value of 0.2.

Setting the external force $f(z,t)$ in Eq. (1) to 0 without considering damping, we obtain

$$EIy''''(z,t) - Ty''(z,t) + m_z\ddot{y}(z,t) = 0 \tag{8}$$

where $'$ represents the derivative of $z$, and $\cdot$ represents the derivative of time $t$.

Using the method of separating variables to solve Eq. (8), the solution based on the mode superposition method is

$$y(z,t) = \sum_{i=1}^{\infty}\psi_i(z)q_i(t) \tag{9}$$

where $\psi_i(z)$ denotes the i-th vibration mode, and $q_i(t)$ represents the amplitude of the i-th vibration that changes with time. Substituting Eq. (9), and the boundary conditions in Eqs. (2)–(4) into Eq. (8), we obtain its eigenvalues and eigenfunctions as

$$\omega_i = \frac{i\pi}{L}\sqrt{\frac{EI}{m_z}\left(\frac{i\pi}{L}\right)^2 + \frac{T}{m_z}} \tag{10}$$

$$\psi_i(z) = \sqrt{\frac{2}{L}}\left(\sin(\alpha z) - \frac{\sin(\alpha L)}{\sinh(\beta L)}\sinh(\beta z)\right) \tag{11}$$

$$\alpha=\sqrt{\sqrt{\frac{m_z\omega_i}{EI}+\frac{1}{4}\left(\frac{T}{EI}\right)^2}-\frac{1}{2}\left(\frac{T}{EI}\right)^2}\quad \beta=\sqrt{\sqrt{\frac{m_z\omega_i}{EI}+\frac{1}{4}\left(\frac{T}{EI}\right)^2}+\frac{1}{2}\left(\frac{T}{EI}\right)^2}$$

Substituting Eq. (9) into Eq. (8), then multiplying each term in Eq. (8) by $\psi_j(z)$, and then integrating 0 to $L$ along the Z direction, we get

$$EI\int_0^L \psi''''_i\psi_j dz - T\int_0^L \psi''_i\psi_j dz - \int_0^L m_z\omega_i^2\psi_i\psi_j dz = 0 \tag{12}$$

The trigonometric functions have orthogonality, and therefore, the shape of vibration $\psi_i(z)$ have the orthogonality

$$\int_0^L \psi_i(z)\psi_j(z)dz = \begin{cases} 0 & i \neq j \\ 1 & i = j \end{cases} \tag{13}$$

We used the principle of virtual work. The governing equations of simply supported beams with a moment $\tau(t)$ at the boundary are established [26].

$$\int_0^L m_z\ddot{y}\delta y dz + \int_0^L (EIy'''' - Ty'')\delta y dz + \int_0^L c\dot{y}\delta y dz = \int_0^L f(z,t)\delta y dz - \tau(t)\delta\left(y'_{z=L}\right) \tag{14}$$

Variational processing on Eq. (9) gives

$$\delta y(z,t) = \sum_{i=1}^{\infty}\psi_i(z)\delta q_i(t) \tag{15}$$

Substituting Eq. (11), Eq. (13), and Eq. (15) into Eq. (14),

$$\sum_{i=1}^{\infty}\left(m_z\ddot{q}_i + c_i\dot{q}_i + m_z\omega_i^2 q_i - \int_0^L f(z,t)\psi_i(z)dz + \tau(t)\psi_i'(L)\right)\delta q_i = 0 \tag{16}$$

where $c_i = 2m_z\omega_i\zeta_i$ and $\zeta_i = \zeta_{si} + \zeta_{hi}$, where $\zeta_i$, $\zeta_{si}$, and $\zeta_{hi}$ denote the modal damping ratio, modal structural damping ratio, and modal hydrodynamic damping ratio.

Here, we consider the first few modes; the infinite series in Eq. (9) can then be truncated into a finite one as

$$y(z,t) = \sum_{i=1}^{N}\psi_i(z)q_i(t) \tag{17}$$

where $N$ represents the number of first several modes considered. Therefore, the partial differential equation (PDF) in Eq. (16) is reduced to $N$ ordinary differential equations (ODEs) as

$$\sum_{i=1}^{N}\left(m_z\ddot{q}_i + c_i\dot{q}_i + m_z\omega_i^2 q_i - \int_0^L f(z,t)\psi_i(z)dz + \tau(t)\psi_i'(L)\right)\delta q_i = 0 \tag{18}$$

### 2.2. Lift coefficient and mode overlap elimination of VIV

The VIV modeling method follows the contents of SHEAR7 V4.4 [25]. However, the fundamental differences from SHEAR7 V4.4 are the lift coefficient curve and the overlap elimination of power-in regions.

The relevant VIV experimental results show that the lift coefficient $C_L(A/D)$ is affected by the amplitude of the riser as shown in Fig. 2. The empirical lift curve obtained through a large number of experiments is adopted by many software packages (SHEAR7,

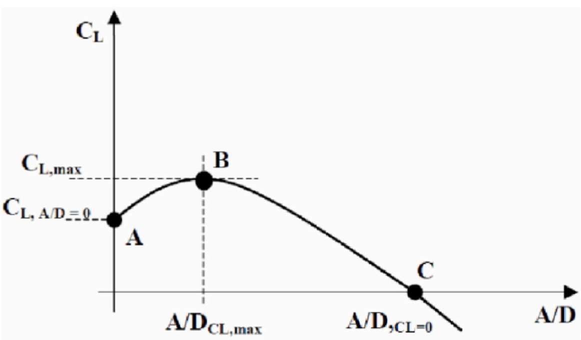


**Fig. 2.** Typical lift coefficient curve.

VIVANA) [25]. However, before the numerical analysis, the amplitude of the riser is unknown, and the lift coefficient can only be obtained by iterative calculation.

To speed up the iteration and maintain stability, the relationship between lift coefficient vs. the A/D curve is represented as a cubic curve instead of two parabolas, which can be expressed as

$$C_L\left(\frac{A}{D}\right)=C_{L0}+a\left(\frac{A}{D}\right)+b\left(\frac{A}{D}\right)^2+c\left(\frac{A}{D}\right)^3 \tag{19}$$

where $C_{L0}$ denotes the initial lift coefficient. Here, $a$, $b$, and $c$ represent the corresponding coefficients. A new lift curve is fitted with the values of the key points (initial value $C_{L0}$, peak value $C_{L\max}A_{\max}$, and $A_0$ when $C_L=0$) of the original lift curve. The solutions of $a$, $b$, and $c$ are

$$a=\frac{3A_0^2C_{L0}-2A_0^3C_{L0}-3A_0^2C_{L0}+2A_0^3C_{L\max}-3A_{\max}^2C_{L0}+2A_{\max}^3C_{L0}}{A_0A_{\max}\left(A_0^2+A_0A_{\max}-3A_0-2A_{\max}^2+3A_{\max}\right)}$$

$$b=\frac{A_0^3C_{L0}-A_0^3C_{L\max}+3A_{\max}^2C_{L0}-A_{\max}^3C_{L0}-3A_0A_{\max}C_{L0}+3A_0A_{\max}C_{L\max}}{A_0A_{\max}^2\left(A_0^2+A_0A_{\max}-3A_0-2A_{\max}^2+3A_{\max}\right)}$$

$$c=\frac{-\left(A_0^2C_{L0}-A_0^2C_{L\max}+A_{\max}^2C_{L0}-2A_0A_{\max}C_{L0}+2A_0A_{\max}C_{L\max}\right)}{A_0A_{\max}^2\left(A_0^2+A_0A_{\max}-3A_0-2A_{\max}^2+3A_{\max}\right)}$$

A sketch of the overlap region excited by the i-th and j-th modes is plotted in Fig. 3. If there is an overlap between adjacent power-in regions, the power-in region length of each mode involved in the overlap shrinks equally until the overlap disappears in SHEAR7. Here, a method is used to reduce the overlap length of each mode by half. Table 1 lists the relationships between the length of the power-in regions.

### 2.3. Prediction of VIV

Assume that in the i-th mode, the input and output power are balanced as

$$\frac{A_i}{D}=\frac{\int_{L^i}\frac{1}{2}\rho C_L\left(\frac{A}{D}\right)U^2(z)|\psi_i(z)|dz}{\int_{L-L^i}R_h(z)\psi_i^2(z)\omega_i dz+\int_0^L R_s(z)\psi_i^2(z)\omega_i dz} \tag{20}$$

where $A_i$ denotes the modal displacement amplitude of the structure for mode $i$. The lift coefficient $C_L(A/D)$ in Eq. (20) is assigned an initial value. Then, the iterative calculation is started, and the simplified lift coefficient curve in Eq. (8) is used to accelerate the convergence speed until the A/D reaches the convergence error, i.e., the error between the previous step A/D and the current step A/D is less than 0.001.

The low reduced velocity damping model is given as

$$R_h=C_{rl}\rho DU(z)+R_{sw}$$

where $C_{rl}$ and $R_{sw}$ denote an empirical coefficient and the still water contribution, respectively.

$$R_{sw}=\frac{\omega\pi\rho D^2}{2}\left(\frac{2\sqrt{2}}{\sqrt{\mathrm{Re}_w}}+C_{sw}\left(\frac{A}{D}\right)^2\right)$$

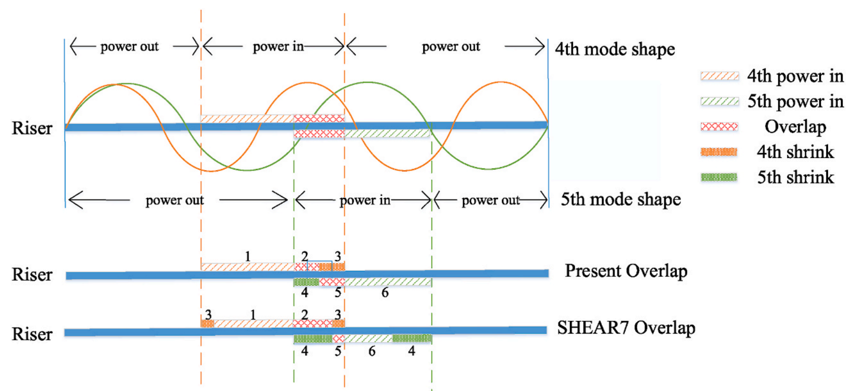


**Fig. 3.** Sketch of overlap region excited by i-th and j-th modes.

**Table 1**
Power-in regions in SHEAR7 and Present method.

| Type | Modes | Power-in regions | Overlap region | Eliminated power-in regions |
|---|---|---|---|---|
| Present | ith | I1+I2 | I2 | P1+P2 |
| Present | jth | I2+I3 | I2 | P5+P6 |
| SHEAR7 4.4 | ith | I1+I2 | I2 | S1+S2 |
| SHEAR7 4.4 | jth | I2+I3 | I2 | S5+S6 |

Note: I1 = P1 = S1 + S3, I2/2.0 = P2 = P3 = P4 = P5, I2 = S2 + S3 = S4 + S5, I3 = P6 = S6 + S4, S2 = S4, S3 = S5. The different methods of eliminating overlapping power-in regions affect the distribution of power-in regions, and thus, the lift coefficient. Furthermore, the numerical results show that the presented approach can provide an acceptable agreement with the experiment.

where $\mathrm{Re}_w = \omega D^2/\nu$, $\nu$ denotes the kinematic viscosity of the fluid.

The high reduced velocity damping model is given by

$$R_h = \frac{C_{rh}\rho U^2(z)}{\omega}$$

where $C_{rh}$ denotes an empirical coefficient.

The modal damping ratio $\zeta_i = \zeta_{hi} + \zeta_{si}$

$$\zeta_{hi} = \frac{\int_{L-L^i} R_h(z)\psi_i^2(z)dz}{2m_z\omega_i}$$

The structural response is included in both the resonant and nonresonant modes [25]. From the mode superposition method, we obtain

$$y(z) = \sum_i^\infty y(z,\omega_i) = \sum_i^\infty \sum_j^\infty \psi_i(z) f_{ji} H_{ji}\left(\frac{\omega_j}{\omega_i}\right) \tag{21}$$

where $y(z)$ and $f_{ji}$ denote the displacement response and the model force, respectively. Further, $H_{ji}(\omega_j/\omega_i)$ represents the frequency response function.

$$f_{ji} = \int_0^L \frac{1}{2}\mathrm{sgn}(\psi_i(z))\psi_j(z)\rho C_L\left(\frac{A}{D}\right)DU^2(z)dz$$

$$\mathrm{sgn}(\psi_i(z)) = \begin{cases} -1 & \psi_i(z) < 0 \\ 0 & \psi_i(z) = 0 \\ 1 & \psi_i(z) > 0 \end{cases} \quad H_{ji}\left(\frac{\omega_j}{\omega_i}\right) = \frac{1}{m_z\omega_i^2}\frac{1}{1-\left(\frac{\omega_j}{\omega_i}\right)^2 + \mathrm{Im}\left(2\zeta_i\frac{\omega_j}{\omega_i}\right)}$$

## 3. Control law design

### 3.1. State-space expressions

Based on the calculation of VIV, we planned to control the participating vibration modes; i.e., $\omega = \{\omega_1, \omega_2, \cdots, \omega_m, \omega_{m+1}, \cdots, \omega_{N-1}, \omega_N\}$, where $N$ denotes the equal total number of participating vibration modes in Eq. (18).

$$\begin{aligned}
&m_z\ddot{q}_1 + c_1\dot{q}_1 + m_z\omega_1^2 q_1 - \int_0^L f(z,t)\psi_1(z)dz + \tau(t)\psi_1'(L) = 0\\
&m_z\ddot{q}_2 + c_2\dot{q}_2 + m_z\omega_2^2 q_2 - \int_0^L f(z,t)\psi_2(z)dz + \tau(t)\psi_2'(L) = 0\\
&\vdots\\
&m_z\ddot{q}_m + c_m\dot{q}_m + m_z\omega_m^2 q_m - \int_0^L f(z,t)\psi_m(z)dz + \tau(t)\psi_m'(L) = 0\\
&m_z\ddot{q}_{m+1} + c_{m+1}\dot{q}_{m+1} + m_z\omega_{m+1}^2 q_{m+1} - \int_0^L f(z,t)\psi_{m+1}(z)dz + \tau(t)\psi_{m+1}'(L) = 0\\
&\vdots\\
&m_z\ddot{q}_{N-1} + c_{N-1}\dot{q}_{N-1} + m_z\omega_{N-1}^2 q_{N-1} - \int_0^L f(z,t)\psi_{N-1}(z)dz + \tau(t)\psi_{N-1}'(L) = 0\\
&m_z\ddot{q}_N + c_N\dot{q}_N + m_z\omega_N^2 q_N - \int_0^L f(z,t)\psi_N(z)dz + \tau(t)\psi_N'(L) = 0
\end{aligned} \tag{22}$$

We discussed the above problem in the state space and let the state vector be $\{x_c\} = [q_1, q_2, \cdots, q_m, q_{m+1}, \cdots, q_{N-1}, q_N, \dot{q}_1, \dot{q}_2, \cdots, \dot{q}_m, \dot{q}_{m+1}, \cdots, \dot{q}_{N-1}, \dot{q}_N]^T$. Further, Eq. (22) can be converted into the state-space form as

$$\begin{cases} \dot{x}_c = Ax_c + Bu + F \\ y = Cx_c \end{cases} \tag{23}$$

where

$$A = \begin{bmatrix} \mathrm{diag}_{N\times N}(0) & \mathrm{diag}_{N\times N}(1) \\ \mathrm{diag}_{N\times N}(-\omega_1^2, -\omega_2^2, \cdots, -\omega_m^2, -\omega_{m+1}^2, \cdots -\omega_{N-1}^2, -\omega_N^2) & \mathrm{diag}_{N\times N}\left(-\frac{c_1}{m_z}, -\frac{c_2}{m_z}, \cdots, -\frac{c_m}{m_z}, -\frac{c_{m+1}}{m_z}, \cdots, -\frac{c_{N-1}}{m_z}, -\frac{c_N}{m_z}\right) \end{bmatrix}_{2N\times 2N},$$

$\mathrm{diag}_{N\times N}$ denotes an N-dimensional diagonal matrix.

$$B = \begin{bmatrix} 0, 0, \cdots, 0, 0, \cdots, 0, 0, -\frac{\psi_1'(L)}{m_z}, -\frac{\psi_2'(L)}{m_z}, \cdots, -\frac{\psi_m'(L)}{m_z}, \\ -\frac{\psi_{m+1}'(L)}{m_z}, \cdots, -\frac{\psi_{N-1}'(L)}{m_z}, -\frac{\psi_N'(L)}{m_z} \end{bmatrix}^T$$

$$F = \begin{bmatrix} 0, 0, \cdots, 0, 0, \cdots, 0, 0, -\frac{\int_0^L f(z,t)\psi_1 dz}{m_z}, -\frac{\int_0^L f(z,t)\psi_2 dz}{m_z}, \cdots, -\frac{\int_0^L f(z,t)\psi_m dz}{m_z}, \\ -\frac{\int_0^L f(z,t)\psi_{m+1} dz}{m_z}, \cdots, -\frac{\int_0^L f(z,t)\psi_{N-1} dz}{m_z}, -\frac{\int_0^L f(z,t)\psi_N dz}{m_z} \end{bmatrix}^T$$

$$C = [\psi_1(z), \psi_2(z), \cdots, \psi_m(z), \psi_{m+1}(z), \cdots, \psi_{N-1}(z), \psi_N(z), 0, 0, \cdots, 0, 0, \cdots, 0, 0]$$

$$u(t) = \tau(t)$$

### 3.2. Control law design through LQR optimization

The LQR cost function is given by

$$J = \frac{1}{2}\int_0^\infty \left[x_c^T(t)Qx_c(t) + u^T(t)Ru(t)\right]dt \tag{24}$$

where $Q$, $R$, and $x_c^T(t)Qx_c(t)$ denote the positive-semi-definite and symmetric matrix, positive-definite weighting and symmetric matrix, and the state response of the entire system. Further, $u^T(t)Ru(t)$ corresponds to the energy cost of the control system. The ratio of $Q$ and $R$ affects the weights of the state response and the required input, and their values significantly affect the final control effect of the closed-loop system. If the matrix elements of $Q$ are weighed, the system response or state $x_c(t)$ will be smaller. Similarly, if the values of $R$ are larger than $Q$, the required control input $u(t)$ will be smaller. Theoretically, this implies that larger values of $Q$ result in poles, and the closed-loop system matrix $(A - BG)$ is left in the s-plane. The state response will then attenuate faster and become smaller. A larger $R$ implies that less control effort is required, and therefore, the poles are generally larger, which results in larger values of the state $x_c(t)$.

For simplicity, $Q$ and $R$ are selected as diagonal matrices. The choices of $Q$ and $R$ are arbitrary, empirical, and not unique. For the specific problem, we compare the results to determine $Q$ and $R$ through the trial calculations of different $Q$ and $R$. To ensure that $Q$ and $R$ have significant physical meaning, we set the values of $Q$ and $R$ as

$$Q = c_{c1} \times \begin{bmatrix} diag_{N\times N}(\omega_1^2, \omega_2^2, \cdots, \omega_m^2, \omega_{m+1}^2, \cdots, \omega_{N-1}^2, \omega_N^2) & diag_{N\times N}(0) \\ diag_{N\times N}(0) & diag_{N\times N}(1) \end{bmatrix}_{2N\times 2N} \quad R = c_{c2}, \tag{25}$$

where $c_{c1}$ and $c_{c2}$ are constants. Substituting Eq. (25) into Eq. (24), we get

$$\int_0^\infty x_c^T(t)Qx_c(t)dt = \int_0^\infty \sum_{i=1}^N c_{c1}\left(\omega_i^2 q_i^2 + \dot{q}_i^2\right)dt \tag{26}$$

$$\int_0^\infty u^T Ru dt = \int_0^\infty c_{c2} u^2 dt \tag{27}$$

Eqs. (26) and (27) represent the entire energy of the system (including the kinetic energy and potential energy) and the energy cost of the active control system, respectively. The ratio $c_{c1}$: $c_{c2}$ determines the weight of the state response and the required input. For simplicity, $c_{c2}$ (i.e., R) is set as 1 [27,28]. Compared to the system without the control, when $c_{c1}$ is relatively small, the bending moment input is small, and this has a little effect on the state response. However, when $c_{c1}$ is large, the bending moment input becomes more extensive, and the state response changes significantly.

The optimal controller is designed to determine the control input $u(t)$ so as to minimize the LQR cost function $J$. To obtain the gain matrix $G$, it is assumed that there exists a constant matrix $P$ given by

$$\frac{d}{dt}\left(x_c^T P x_c\right) = -x_c^T\left(Q + G^T R G\right)x_c \tag{28}$$

Then, substituting Eq. (28) into Eq. (24) yields

$$J = -\frac{1}{2}\int_0^{\infty}\frac{d}{dt}\left(x_c^T P x_c\right)dt = \frac{1}{2}x_c^T(0) Q x_c(0) \tag{29}$$

where $u(t) = -Gx_c(t)$. The closed-loop system should be stable so that $x_c(t)$ moves to its original position as time $t$ changes. Eq. (29) suggests that $J$ is a constant that depends only on matrix $P$ and the initial conditions. To differentiate Eq. (28) and substitute into $\dot{x}_c = (A - BG)x_c$, Eq. (28) can be rewritten as

$$\dot{x}_c^T P x_c + x_c^T P \dot{x}_c + x_c^T Q x_c + x_c^T G^T R G x_c = 0 \;\; or \;\; x_c^T\left((A - BG)^T P + P(A - BG) + Q + G^T R G\right)x_c = 0$$

$$A^T P + PA + Q + G^T R G - G^T B^T P - PBG = 0 \tag{30}$$

Eq. (30) denotes a matrix quadratic equation. After setting $G = R^{-1}B^T P$, we have

$$PA + A^T P - PBR^{-1}B^T P + Q = 0 \tag{31}$$

Eq. (31) denotes the algebraic Riccati equation (ARE), and matrix $P$ denotes the positive semi-definite solution. Because $Q$ is positive-semi-definite and $R$ is positive-definite, matrix $P$ is available. Next, the closed-loop system $(A - BG)$ is asymptotically stable.

Substituting $u(t)$ into Eq. (23), we can obtain the state equations of the closed-loop system

$$\begin{cases} \dot{x}_c = (A - BG)x_c + F \\ y = Ck \end{cases} \tag{32}$$

As there are many calculation processes, the entire calculation process is shown in Fig. 4. The primary process is described as follows. First, the VIV of the riser is calculated in the frequency domain to determine the distribution of lift coefficients and damping coefficients along the riser. Then, the dynamic system is transformed into a time-domain state equation, and the lift and damping forces—obtained by calculating the distribution of lift coefficients and damping coefficient along the riser—are applied to the riser. Finally, the LQR optimal controller applies a bending moment at the riser's top end to reduce the top corner and VIV vibration displacement. The lift coefficient distribution remains unchanged during the control process to facilitate the solution of the algebraic Riccati equation of the LQR state equation.

## 4. Numeric analysis and discussions

### 4.1. VIV response of original system

To verify the effectiveness of the proposed approach, the results are compared with SHEAR7 4.3e [29]. The Mechanical properties of the riser are listed in Table 2. The transverse force was simulated using the oscillating lift $F_L(z,t)$ in Eq. (6) with the initial value $C_{L0}$

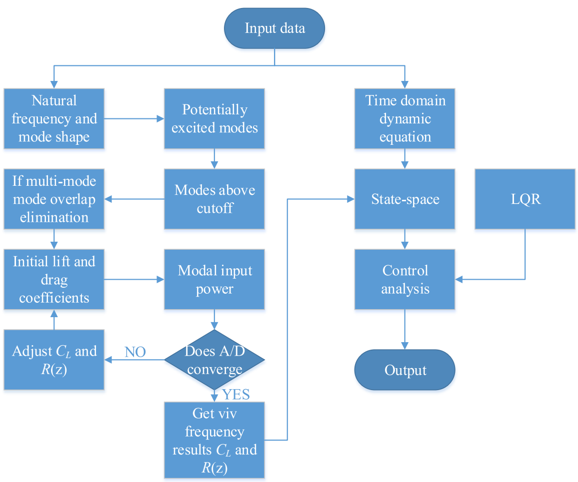


**Fig. 4.** Flowchart of the LQR designing of riser VIV.

$= 0.3$, peak value $C_{Lmax} = 0.70$ when $A_{\max} = 0.3$, zero position $A_0 = 1.1$. $S_t = 0.18$ was adopted for the subcritical flow. $U$(z) denote the shear current, velocity at the top of the riser is $U(L) = U_{Top} = 0.9144$ m/s, and the velocity at the bottom of the riser is $U(0) = U_{Bottom} = 0.3048$ m/s $C_{rl} = 0.18$, $C_{sw} = 0.2$, and $C_{rh} = 0.2$. The cut-off for eliminating unimportant modes was set to 0.1.

A comparison of the eigenvalues is illustrated in Fig. 5; the error is small, and the maximum error is 1% in the 21st mode. A comparison of the lift force coefficient in the power-in region between SHEAR7 and the presented approach is shown in Fig. 6. According to the cut-off value (0.1) of the elimination mode, several modes (modes 9, 10, 11, 12, 13, and 14) involved in the vibration are defined.

The length of the modal power-in region determines the distribution length of the modal lift coefficient, and the value of the lift coefficient corresponds to the mode shape of the modal power-in region. The node of the vibration mode shape (0 amplitude) at the position where the vibration mode intersects with 0 in the lateral direction, and the lift coefficient at $A_0$ in the lift curve is $C_{L0}$. The antinode of the vibration mode is the maximum amplitude, which is the maximum or minimum value of the lift curve in the vibration mode, and its lift coefficient needs to be calculated iteratively.

The results of the dominant excited mode and length of the lift force coefficient as predicted by the proposed method are the same as those obtained using SHEAR7. However, compared with the position of the lift coefficient of the presented approach, the position of the same excitation mode of SHEAR7 is closer to the top of the riser, and the values of the lift coefficient are larger than those of the present method. The lift coefficient curves are different: a cubic curve in this study and two parabolas in SHEAR7. In this case, the cubic curve overestimates the lift coefficient, i.e., the peak value is 0.90 at A/D = 0.6. Further, there is an overlap between the adjacent power-in regions; the different overlapping elimination methods affect the length of the power-in regions, which affects the lift coefficient. A comparison of the nondimensional root mean square (RMS) displacement and RMS acceleration is shown in Figs. 7 and 8, respectively. The values in SHEAR7 are in general agreement with the values in the proposed approach in this example. The maximum RMS displacement is 8.9% larger than that of SHEAR7. Moreover, the maximum RMS acceleration is more massive (approximately 9.8%) than that of SHEAR7.

The second verification is a comparison with the experimental results [30]. The riser parameters are listed in Table 3. The initial value $C_{L0} = 0.5$, the peak value $C_{Lmax} = 0.75$ when $A_{\max} = 0.35$, and the zero position $A_0 = 1.1$. The cubic curve fits the lift coefficient well. Moreover, other data are the same as in the above example.

The RMS displacement under shear current (the velocity at the top of the riser is $U_{Top} = 2.4$ m/s and $U_{Top} = 3.2$ m/s; the velocity at the bottom of the riser is $U_{Bottom} = 0$ m/s) is shown in Figs. 9 and 10, respectively. The experimental results of the displacement are in agreement with the numerical results in this example. Moreover, the maximum displacement differed by 10%; thus, the accuracy of the numerical prediction of VIV is acceptable.

### 4.2. Active suppression based on LQR controller

The VIV of a marine riser is suppressed by applying the LQR controller. The number model riser is a typical marine top tensioned riser (TTR). The system parameters [21] are listed in Table 4. $U(z)$ denotes the shear current, $U_{Top} = 0.9$ m/s, and $U_{Bottom} = 0$ m/s. $C_{L0} = 0.5$, $C_{Lmax} = 0.75$ when $A_{\max} = 0.35$, and $A_0 = 1.1$. The initial state of the riser is stationary. The time-domain analysis adopts the explicit fourth-order Runge–Kutta method with a time step of 0.05 s.

We present the simulation results of the closed-loop control system (CLCS) and the original system (OS). Here, the CLCS is the dynamics system of the riser with bending moment input $\tau(t)$ control, while the OS is the dynamic system of the riser without the bending moment input $\tau(t)$ control.

The estimated input power ratios in the second, third, fourth, and fifth modes are 0.0084, 0.0936, 1, and 0.0120, respectively, while the input power ratios in the other modes are close to zero. Since the cut-off value is 0.1, the potentially excited mode is modal four, as shown in Fig. 11. Only one mode is excited, and therefore, the reduced velocity bandwidth $\Delta U_B$ is 0.4. The RMS displacement in Fig. 12 shows that mode four is the dominant mode, where there are four peaks. The maximum peak is close to the top of the riser.

#### 4.2.1. Mode-weighted control vs. mode-averaged control

The vibration of the riser not only has a resonance mode contribution but also a nonresonance mode contribution. Therefore, Case A, which is mode-weighted control (excited mode, mode four), and Case B, which is mode-averaged control (the first ten modes), are considered during the LQR active control. In Cases A and B, only parameter Q is different, and the other parameters are the same. Q represents a 20 × 20 matrix. On substituting Eq. (26), one can obtain.

Case A:

**Table 2**
Mechanical properties of the riser.

| Parameters of the physical system | Value | Units |
|---|---|---|
| Length of riser ($L$) | 60.96 | m |
| Mass per unit length ($m_z$) | 2.0313 | kg/m |
| Outer diameter ($D$) | 0.033274 | m |
| Sea water density ($\rho$) | 1024 | kg/m$^3$ |
| Structural modal damping ratio ($\zeta_s$) | 0.3% | 1 |
| Tension ($T$) | 3558.5776 | N |
| Flexural rigidity ($EI$) | 425.754 | Nm$^2$ |

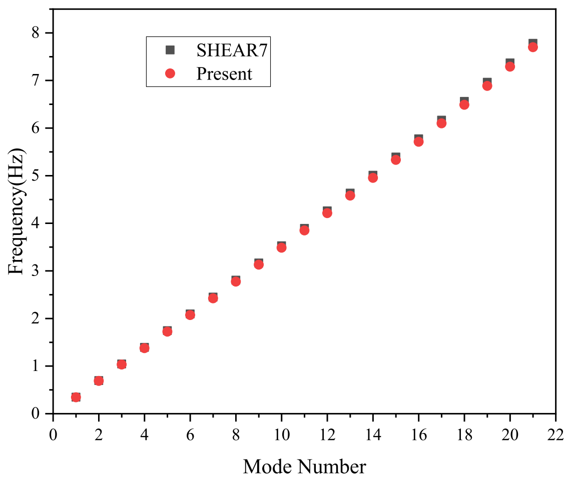


**Fig. 5.** Eigenvalue.

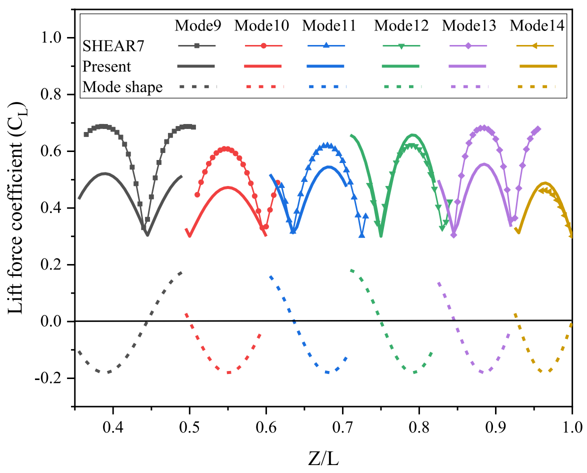


**Fig. 6.** Lift force coefficient.

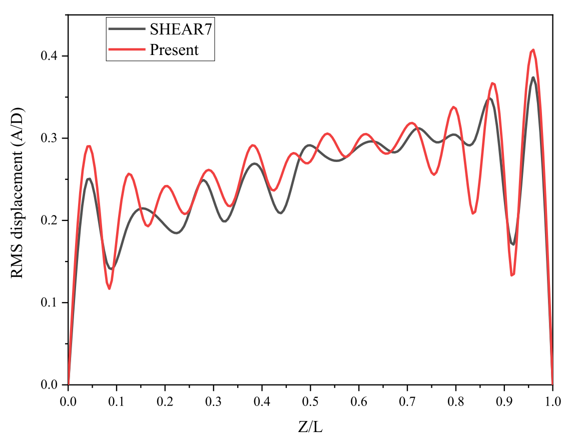


**Fig. 7.** RMS displacement (A/D).

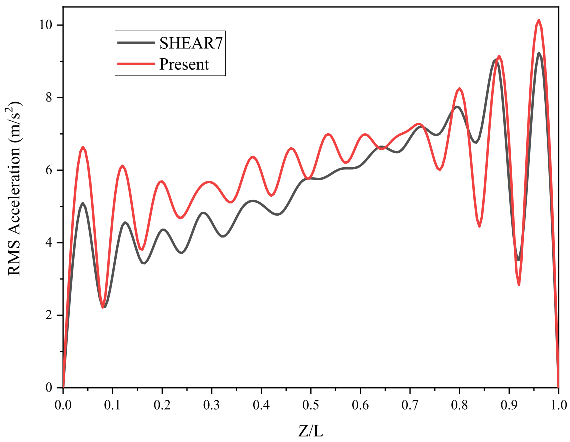


**Fig. 8.** RMS acceleration(m/s$^2$).

**Table 3**
Riser model properties.

| Parameters of the physical system | Value | Units |
|---|---|---|
| Length of riser ($L$) | 6.75 | m |
| Mass per unit length ($m_z$) | 2.4869 | kg/m |
| Outer diameter ($D$) | 0.03 | m |
| Sea water density ($\rho$) | 1000 | kg/m$^3$ |
| Structural modal damping ratio ($\zeta_s$) | 0.3% | 1 |
| Tension ($T$) | 3000 | N |
| Flexural rigidity ($EI$) | 1476.76 | Nm$^2$ |

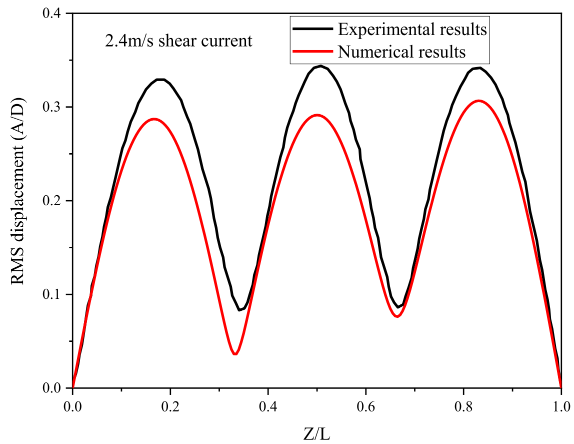


**Fig. 9.** RMS displacement (A/D, $U_{\text{Top}} = 2.4$ m/s).

$$Q = \begin{bmatrix} diag_{10\times10}(0,0,0,\omega_4^2,0,0,0,0,0,0) & [0]_{10\times10} \\ [0]_{10\times10} & diag_{10\times10}(0,0,0,1,0,0,0,0,0,0) \end{bmatrix} \times c_{c1},$$

Case B:

$$Q = \begin{bmatrix} \text{diag}_{10\times10}(\omega_1^2,\omega_2^2,\omega_3^2,\omega_4^2,\omega_5^2,\omega_6^2,\omega_7^2,\omega_8^2,\omega_9^2,\omega_{10}^2) & [0]_{10\times10} \\ [0]_{10\times10} & \text{diag}_{10\times10}(1,1,1,1,1,1,1,1,1,1) \end{bmatrix} \times c_{c1}.$$

Therefore, based on Eq. (27); Case A: $\int_0^\infty k^T Qkdt = \int_0^\infty c_{c1}(\omega_4^2 q_4^2 + \dot{q}_4^2)dt$ and Case B: $\int_0^\infty k^T Qkdt = \int_0^\infty c_{c1}\sum_{i=1}^{10}(\omega_i^2 q_i^2 + \dot{q}_i^2)dt$. The entire energy of the system in Case B is greater than that in Case A. In the gain matrix $G$ of Case A, the fourth and fourteenth values (i.e. $q_4$, $\dot{q}_4$ of the variable $k$ position) are more abundant, and other values are close to 0. In the gain matrix $G$ of Case B, all values are more

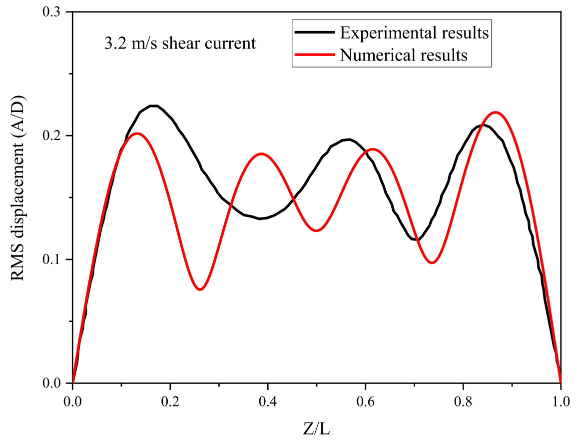


**Fig. 10.** RMS displacement (A/D, $U_{Top} = 3.2$ m/s).

**Table 4**
Numerical values of the system parameters.

| Parameters of the physical system | Value | Units |
|---|---|---|
| Length of riser ($L$) | 1000 | M |
| Mass per unit length ($m_z$) | 15 | kg/m |
| Outer diameter ($D$) | 0.2 | M |
| Sea water density ($\rho$) | 1024 | kg/m$^3$ |
| Structural modal damping ratio ($\zeta_s$) | 0.3% | 1 |
| Tension ($T$) | $1.2 \times 10^6$ | N |
| Flexural rigidity ($EI$) | $4 \times 10^9$ | Nm$^2$ |

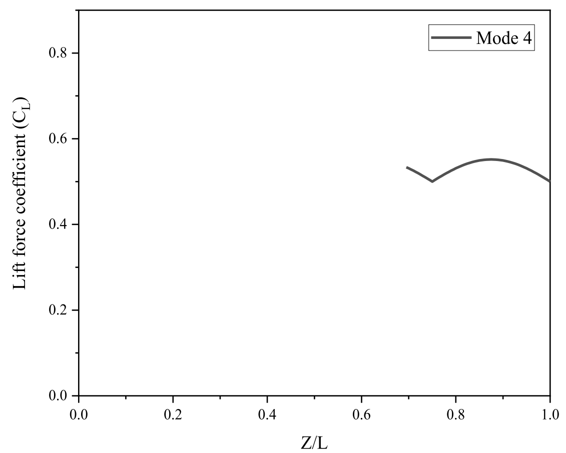


**Fig. 11.** Lift force coefficient.

significant; however, the fourth and fourteenth values are smaller than those in Case A. Therefore, the gain matrix G of Case B couples the set of decoupled equations, thereby reducing the energy proportion of mode four in the entire energy of the system compared with that for Case A.

Next, the coefficient $c_{c2}$ is equal to 1. To find $c_{c1}$, we can perform trial calculations on $c_{c1} = 10^5$, $10^8$, $10^{11}$, and $10^{14}$ in Case B. The calculation results are shown in Fig. 13. The results show that when $c_{c1} = 10^5$, the displacement is almost unchanged. When $c_{c1} = 10^8$, the maximum displacement is 75% of the maximum displacement without control. When $c_{c1} = 10^{14}$, the numerical results (displacement) of the explicit fourth-order Runge–Kutta method are divergent because the eigenvalue ratio $|\lambda_{max} / \lambda_{min}|$ of the CLCS matrix $(A - BG)$ is considerably greater than 1. The state equation at $c_{c1} = 10^{14}$ is a stiff equation that introduces difficulties in the numerical solution, and therefore, it is not considered here. Finally, $c_{c1} = 10^{11}$ was selected; it can be seen that $c_{c1} = 10^{11}$ is optimal in these four cases and does not represent the global optimal.

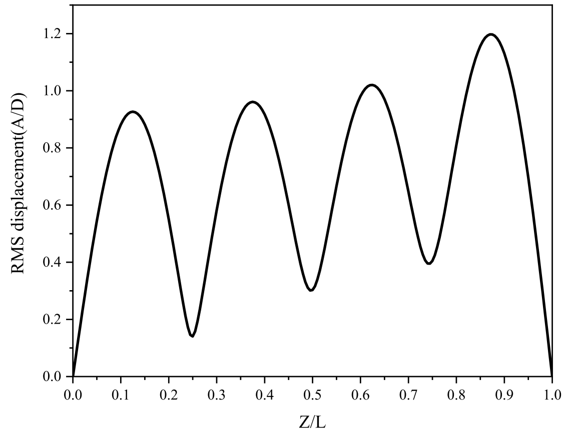


**Fig. 12.** RMS displacement (A/D).

We used matrix eigenvalues to explain the reasons for the different effects of VIV control. The typical eigenvalues of OS and CLCS, i.e., those of matrix $A$ of the OS and $(A - BG)$ of the CLCS, are calculated and compared in Fig. 14. The figure indicates that the CLCS of the mode-weighted control obviously changes the natural frequency of mode four, whereas the CLCS of the mode-averaged control modifies not only changes the frequency of mode four but also those of modes two–three, and five–ten. However, the eigenvalue of mode four of the CLCS using mode-weighted control is much smaller than that of mode-averaged control, and this indicates that the former control has a better suppression effect on mode four than the latter. This can be proved in the following results in Figs. 18 and 19.

The time domain of the bending moment input $\tau(t)$ at the top end of the riser and its frequency domain from fast Fourier transform (FFT) are shown in Figs. 15 and 16. The $\tau(t)$ value of the CLCS of the mode-weighted control and that of the mode-averaged control is a sine function among the range of $(-4.5 \times 10^5, 4.5 \times 10^5)$ N·m and $(-2.5 \times 10^5, 2.5 \times 10^5)$ N·m, respectively. The dominant vibration frequency of the bending moment input is the fourth natural vibration frequency of the riser; i.e., only one peak value $4.5 \times 10^5$ N·m·Hz$^{-1}$, which is located on the fourth natural vibration frequency of the riser in the CLCS of mode-weighted control. The value of $\tau(t)$ is close to zero at other frequencies.

In the CLCS of the mode-averaged control, the maximum peak value is $2.5 \times 10^5$ N m Hz$^{-1}$, which is approximately 56% of the CLCS of mode-weighted control. This is because the eigenvalue of mode four of the CLCS of mode-averaged control is considerably larger than that of the CLCS of mode-weighted control, which is closer to the resonance frequency of mode four.

To quantify the control effect, the control reduction ratio $\eta$ is defined here as $\eta = 1 - \frac{E_{CLCS\max}}{E_{OS\max}}$, where $E_{CLCS\max}$ denotes the maximum displacement or angle of the CLCS, and $E_{OS\max}$ denotes the maximum displacement or angle of the OS. The larger the control reduction ratio $\eta$, the closer to 100%, the better is the control effect.

The top riser angles under three cases including the OS, CLCS of mode-weighted control, and CLCS of mode-averaged control, are shown in Fig. 17. The angle of the OS and mode-averaged control are in the range of $(-8.1 \times 10^{-4}, 8.1 \times 10^{-4})$ rad, $(-2.4 \times 10^{-4}, 2.4 \times 10^{-4})$ rad. The top riser angle of the CLCS of mode-weighted control is less than that of the mode-averaged control CLCS. Further, the

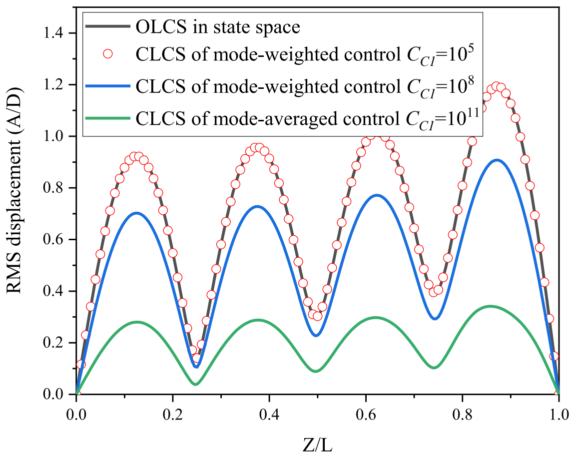


**Fig. 13.** RMS displacement (A/D).

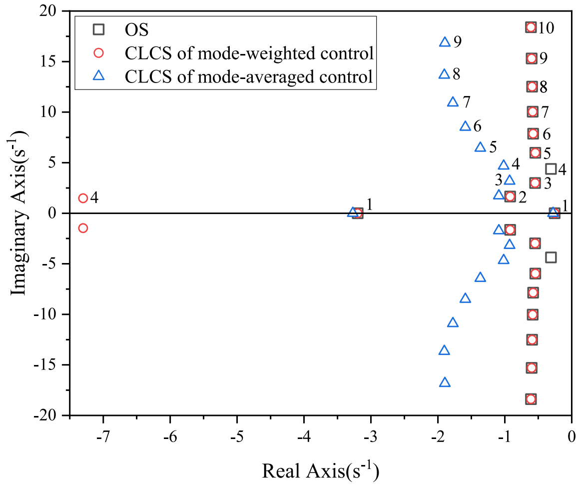


**Fig. 14.** Typical eigenvalues in complex space (Label number indicates the order of the mode.).

top riser angle is significantly suppressed (by approximately $\eta = 89\%$) when the CLCS of mode-weighted control is applied.

The RMS displacements are shown in Fig. 18. In the OS, the displacements calculated in the frequency and time domains by the proposed method are the same. The CLCS of mode-weighted control and that of the mode-averaged control can restrain the vibration displacement. Compared with the OS, the maximum displacements of Cases A and B become 20% and 29% of the maximum displacements of the OS, respectively. In Case A, the maximum displacement is located at Z/L = 0.93, which is close to 9/10 (the antinode of mode five). Five peaks decrease rapidly from the top to the bottom of the riser. In Case B, the maximum displacement is located at Z/L = 0.86, which is close to 7/8 (the antinode of mode four). Four peaks decrease slowly from the top to the bottom of the riser. The dominant mode of Case A (blue curve) changes from mode four to mode five; however, the dominant mode of Case B (green curve) is still mode four as shown in Fig. 19. Further, Fig. 19 demonstrates the dimensionless RMS amplitudes of the first ten modes of the OS and CLCS.

Thus, compared with the OS, the mode-averaged and mode-weighted controls can effectively reduce the displacement and angle by 71%–80% and 70%–89%, respectively. The control reduction stage $\eta$ of the displacement and angle of the presented mode-weighted control is respectively 1.13 and 1.27 times that of the mode-averaged control. In other words, when the VIV lift coefficient distribution is constant, the presented mode-weighted control is more effective than the mode-averaged control for multimode control. The energy of the control input is concentrated on only one mode, while the control energy of the mode-averaged control is distributed evenly to multiple modes. For VIV control with a couple of modes excited during the dynamic response, we can say that mode-weighted control would be better than the mode-averaged control.

The displacements and dominant frequencies at different points along the riser span were examined. Two specific points, i.e., z = 500 (z = 1/2 L) and z = 875 (z = 7/8 L), were taken as examples. They respectively correspond to the node and antinode of mode four, respectively. Fig. 20 shows the displacement and its spectrum; the maximum displacement of the CLCS of the mode-averaged control decreases by approximately $\eta = 70\%$ at z = 500 compared with the OS. Furthermore, the maximum displacement of the CLCS of the mode-weighted control decreases by approximately $\eta = 91\%$ at z = 500 compared with the OS. The CLCS of the mode-averaged control and the CLCS of the mode-weighted control reduces the vibration displacement at z = 875; its control effect at z = 875 is as good as that at z = 500.

The corresponding results in frequency domain are shown in Fig. 20. At z = 500 and z = 875, the responses of mode four are significantly suppressed. At z = 500, the fourth vibration amplitudes of the CLCS of the mode-weighted and mode-averaged controls are approximately 10% and 31% of the OS, respectively. At z = 875, the fourth vibration amplitude of the CLCS of the mode-weighted control and mode-averaged control are approximately 9% and 29% of the OS, respectively. Both the fourth vibration amplitude of the CLCS of the mode-weighted control and mode-averaged control decreases. Because the vibration locking frequency of the riser is at mode 4, z = 500 and z = 875 are the node and antinode of the fourth mode shape, and the vibration amplitude at z = 875 is more significant than that at z = 500. Thus, the CLCS of the mode-weighted control is better than that of mode-averaged control.

#### *4.2.2. Influences of flow currents on closed-systems*

Next, we analyze the influence of speed on the control effect of the CLCS of the mode-weighted control. Lift force coefficients are shown under different flow currents (shear flow, the velocity at the top is $U_{Top1} = 0.9$ m/s, $U_{Top2} = 1.5$ m/s, $U_{Top3} = 2.0$ m/s, the velocity at the end is $U_{Bottom} = 0$ m/s) in Fig. 21. The 0.9 m/s excited mode is only mode 4, and the reduced velocity bandwidth, $\Delta U_B$, is 0.4. The 1.5 m/s and 2.0 m/s excited mode are modes five and six, modes six and seven, respectively. Therefore, the reduced velocity bandwidth $\Delta U_B$ of each excited mode is 0.2. Although the sum of the reduced velocity bandwidths $\Delta U_B$ of the three flow currents is 0.4, the power input region of 0.9 m/s is larger than the power input regions of others. The power input region of 1.5 m/s and 2.0 m/s are similar in location and in length. The response frequency and responding mode number increase when the excitation current becomes

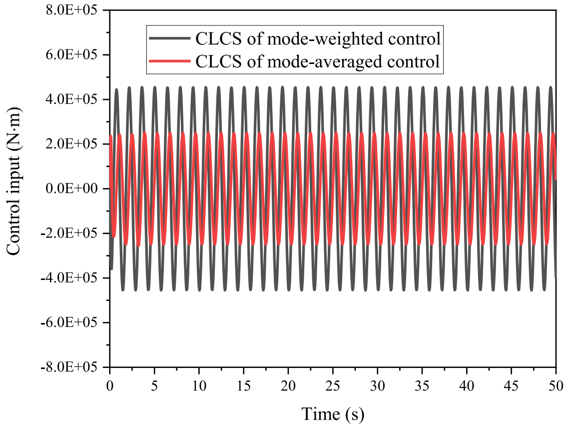


**Fig. 15.** Control input moment at the top end in time domain.

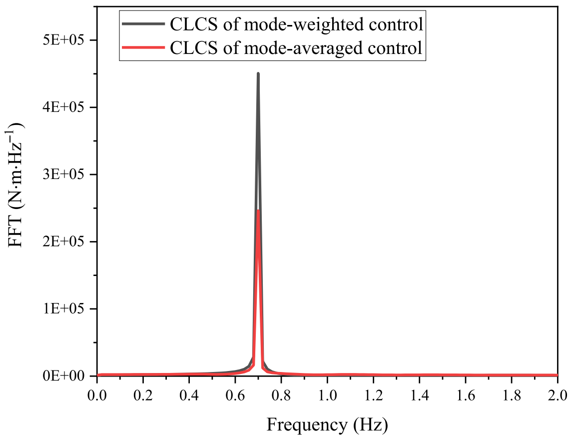


**Fig. 16.** Control input moment at the top end in frequency domain.

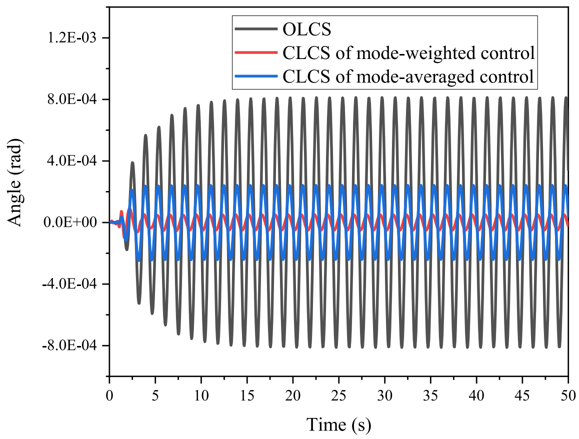


**Fig. 17.** Top angle $y'(L,t)$ of the riser for the original system and closed-loop control system.

faster under Strouhal's law in VIV modeling.

Fig. 22 shows that the RMS displacement of the 0.9 m/s is the maximum, and the RMS displacement of 1.5 m/s and 2.0 ;m/s are approximately at the same level. The main reason is that the length of the power input region of 0.9 m/s is longer than that of the power

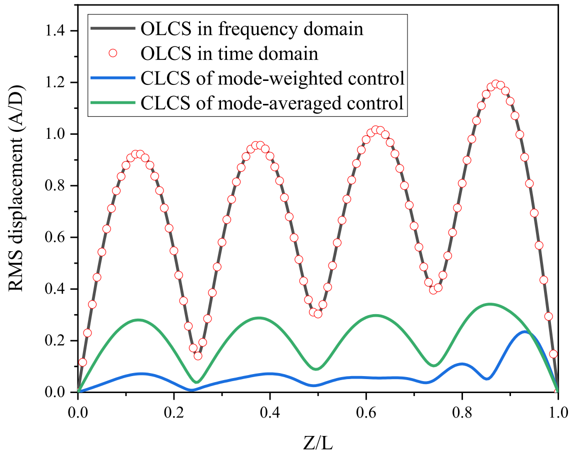


**Fig. 18.** RMS displacement (A/D).

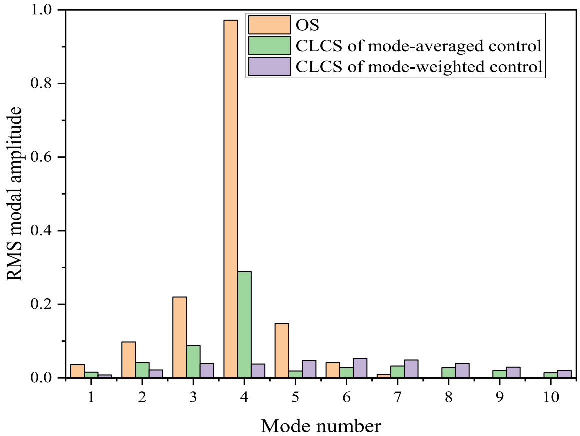


**Fig. 19.** RMS modal amplitude versus mode number.

input region of 1.5 m/s or 2.0 m/s; however, the power input region of 0.9 m/s has only the fourth mode control without the phase difference, whereas the power input region of 1.5 m/s or 2.0 m/s has two mode control with a phase difference. The phase difference leads to the mutual hydrodynamic damping in the energy input region of the two modes that reduces the energy input and increases the energy consumption, thereby reducing the displacement. The displacement at a velocity of 1.5 m/s is not considerably different from that at a velocity of 2.0 m/s. This is because the energy input and energy consumption are similar.

The results show that, with an increase in flow velocity, more higher-order modes are excited, and the VIV response of the original system slightly decreases while the response frequency gradually increases.

The control input moment $\tau$(t) at the top end at 0.9 m/s, 1.5 m/s, and 2.0 m/s are shown in Fig. 23. The moment at 2.0 ;m/s is larger than that at other flow currents. The moment at 0.9 m/s is the smallest, and it is around 36% of the moment at 2.0 m/s. The results of the bending moment input $\tau(t)$ at the top end of the riser in frequency domain are different at 0.9 m/s, 1.5 m/s, and 2.0 m/s, as shown in Fig. 24. The peak at 0.9 m/s is located in the fourth mode of the riser, and peaks at 1.5 m/s are located in the fifth and sixth modes of the riser. The peaks at 2.0 ;m/s are located in the sixth and seventh modes of the riser, and the peak is the highest in the excited higher mode.

The results reveal that with an increase in flow velocity, the proportion of higher frequency vibration in the entire vibration increases. Thus, the maximum value of the input bending moment moves from the low modal frequency to the high modal frequency.

The top riser angles $y'(L,t)$ for CLCS and OS at 0.9 m/s, 1.5 m/s, and 2.0 m/s are shown in Fig. 25. With an increase in flow velocity in both CLCS and OS, the amplitude of the top riser angle decreases, and the frequency of the top angle vibration increases. Compared with the OS, the top riser angle $y'(L,t)$ of CLCS is significantly decreased, and it is reduced by approximately $\eta = 89\%$, 82%, and 81% in the three cases. The control effect decreased as the flow velocity increased.

Fig. 26 shows the nondimensional RMS displacement with different velocities. The displacements of the OS in the frequency response are the same as those of the OS in the state space. This implies the presented state-space equations are satisfied.

The displacement of the CLCS is smaller than that of the OS. In addition, the number of displacement peaks of CLCS is different from

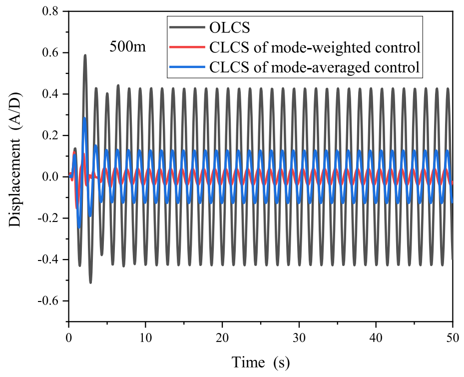


a. Displacement (A/D) at 500 m in time domain

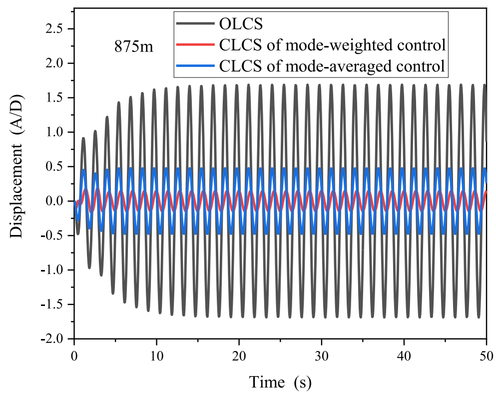


c. Displacement (A/D) at 875 m in time domain

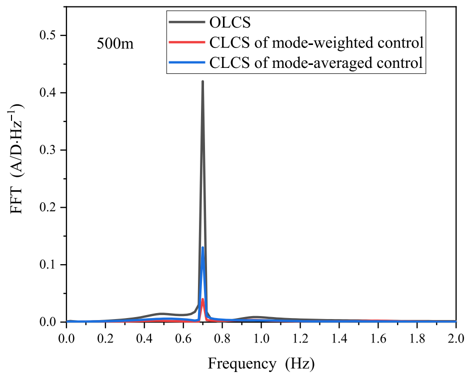


b. Amplitude ($A/D\cdot Hz^{-1}$) at Z = 500 m in frequency domain

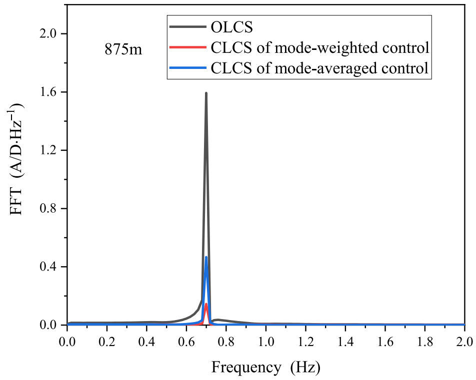


d. Amplitude ($A/D\cdot Hz^{-1}$) at Z = 875 m in frequency domain

**Fig. 20.** Riser displacement of the original and closed-loop systems.

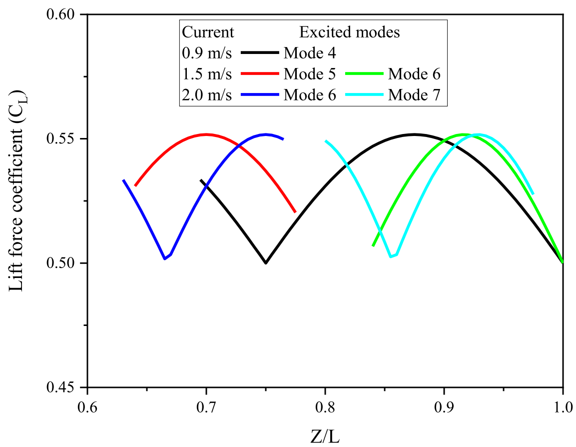


**Fig. 21.** Lift force coefficient.

that of OS. Hence, the dominant control modes were effectively suppressed. $U_{Top1} = 0.9$ m/s, $U_{Top2} = 1.5$ m/s, and $U_{Top3} = 2.0$ m/s; the number of displacement peaks of CLCS changes from four, six, and seven of the OS to five, eight, and nine, respectively. The structural response includes the resonant and nonresonant modes [25]; however, the dominant mode is successfully suppressed, and the

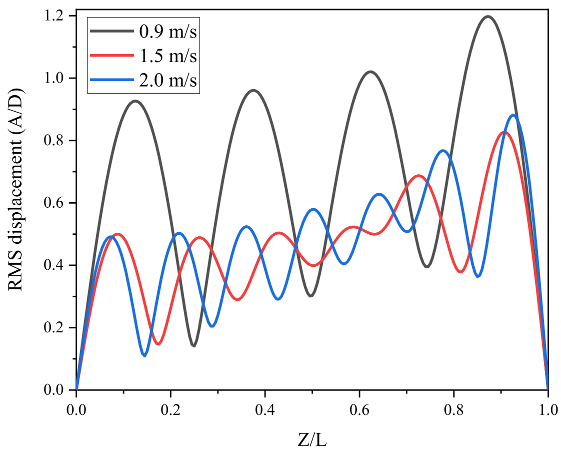


**Fig. 22.** RMS displacement (A/D).

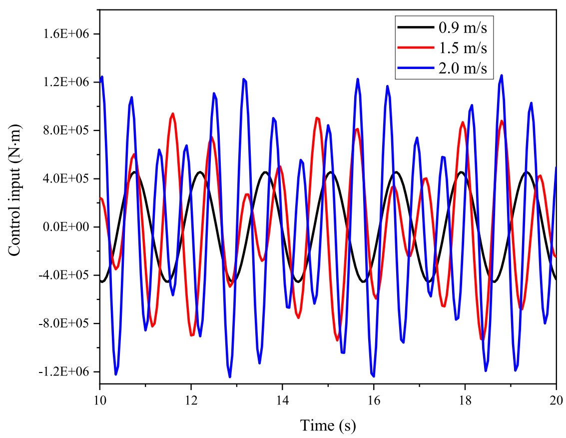


**Fig. 23.** Control input moment at the top end in time domain.

contribution of other modes may become larger (see Figs. 19, 27 and 28). The amplitudes of modes six, seven, and eight are slightly larger than those of the OS, and, the amplitude of mode 5 becomes larger than that of mode four at flow velocity $U_{Top1} = 0.9$ m/s. In this case, mode 5 becomes the dominant mode, instead of mode four in the OS. The final response of the VIV displacement is a combination

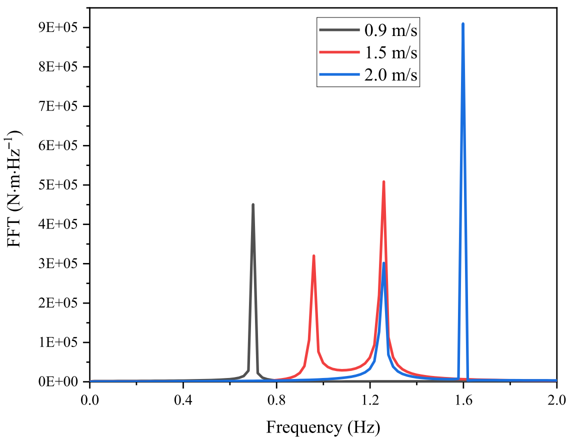


**Fig. 24.** Control input moment at the top end in frequency domain.

of the first ten modes.

One crucial observation should is that at 1.5 m/s and 2.0 m/s, the maximum displacement of CLCS appears at the second peak, while the maximum of the OS is at the first peak. Displacement peaks are ordered from the top to the bottom of the riser. The location of the maximum fatigue damage moves downward from the upper part of the riser, which deserves our attention.

The maximum displacement at 0.9 m/s is the smallest in the CLCS among the three velocities. The control reduction ratio $\eta$ of displacement is equal to 80%, 57%, and 69% at 0.9 m/s, 1.5 m/s, and 2.0 ;m/s, respectively. Therefore, the control effect is the best at 0.9 m/s, followed by the control effect at 2.0 m/s; the worst is at 1.5 m/s in Fig. 29. At different velocities, the decrease in the angle is slightly greater than the decrease in the displacement. In other words, angular control is easier to implement than displacement control, which is expected because the angle at the top of the riser is closer to controlling the bending moment; the controlled displacement is the maximum displacement of the full length of the riser.

## 5. Conclusion

The active control of the flexible riser's multimode VIV in shear flow is studied through the LQR controller. Dynamic models of both the original system and closed-loop system, i.e., the riser with active bending control to the top-end angle, were developed. Further, the approach of LQR designing for a riser VIV with the assumption that the lift coefficient distribution is constant is presented. The responses of closed-loop systems with mode-weighted and mode-averaged approaches are compared with the original systems. The numerical results show that our approach can effectively suppress the response level of riser VIV. The main conclusions can be summarized as follows:

1. Compared with the OS, the displacement and angle of the CLCS are significantly reduced. The case study shows that compared with the original system, the designed active control approaches can effectively reduce displacement and angle (by 71%–80% and 70%–89%, respectively).
2. The presented mode-weighted control was more effective than the mode-averaged control because the input energy contributed to the dominant mode of the multimode VIV response. Furthermore, the case study showed that the displacement and angle drops by 72% and 67%, respectively. Alternatively, the decreases in the displacement and angle can be respectively 1.13 and 1.27 times of the mode-averaged control.
3. The effect of the LQR control can be affected by flow velocity. With an increase in flow velocity, the effect of the LQR control changes. In particular, as the flow velocity rises from 0.9 m/s to 2.0 m/s, the control effect is the best at 0.9 m/s, e.g., the displacement decreases by 80%, while the control effect approaches the lowest at 1.5 m/s. Further, the maximum displacement approaches the smallest value at 0.9 m/s velocity. Therefore, for the VIV of the closed-loop system, the response can be suppressed, the control effect becomes slightly complicated, or the efficiency of the controller may be lower at a certain flow velocity.

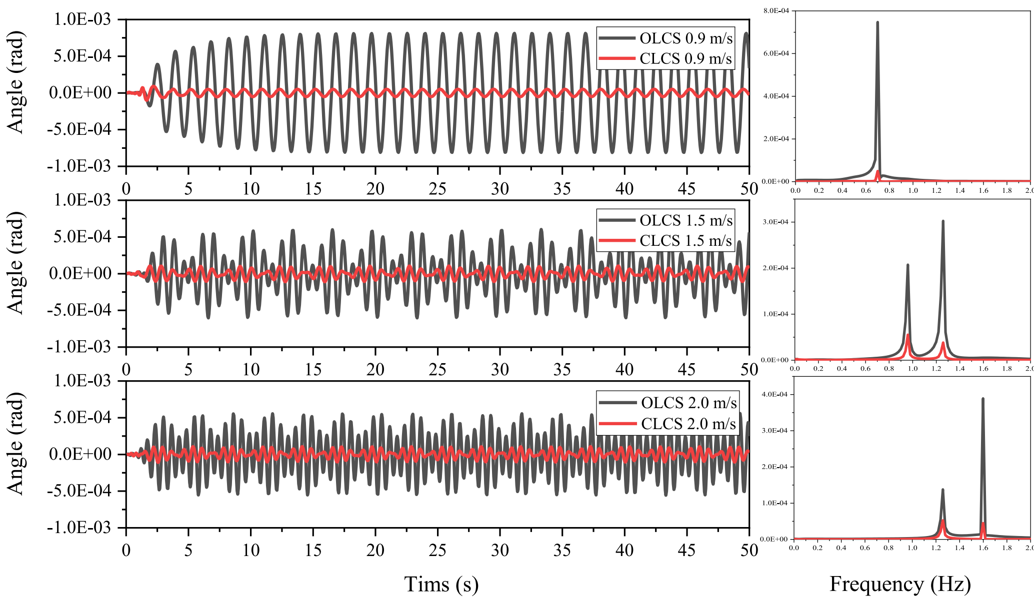


**Fig. 25.** Top riser angle $y'(L,t)$ for the original and closed-loop system.

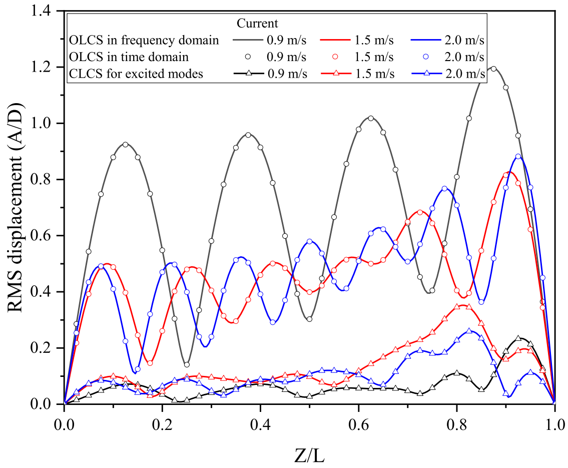


**Fig. 26.** RMS displacement (A/D).

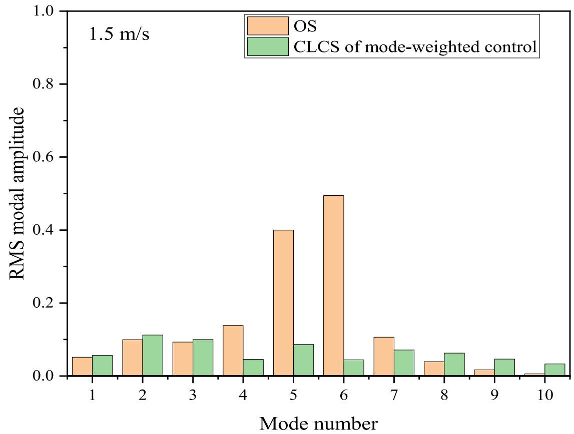


**Fig. 27.** RMS modal amplitude versus mode number.

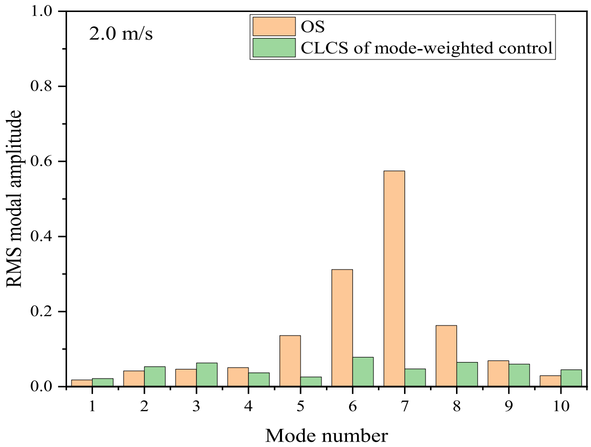


**Fig. 28.** RMS modal amplitude versus mode number.

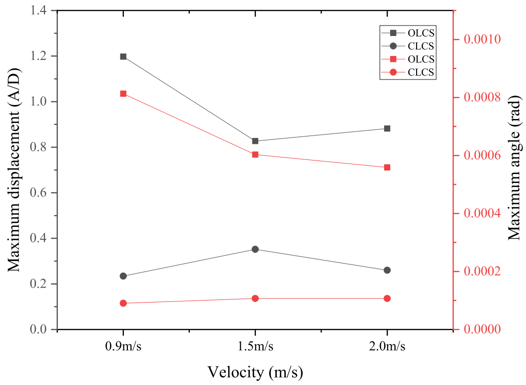


**Fig. 29.** Maximum displacement and maximum angle.

## Declaration of competing interest

The authors declare that they have no conflict of interest.


## Acknowledgments

This work was supported by the Strategic Priority Research Program of the Chinese Academy of Sciences (Grant No. XDA22000000). The authors are grateful for the assistance of the anonymous reviewers.


## References


[1] Williams JE, Zhao BC. The active control of vortex shedding. J Fluid Struct 1989;3:115–22.
[2] He JW, Glowinski R, Metcalfe R, Nordlander A, Periaux J. Active control and drag optimization for flow past a circular cylinder: I. Oscillatory cylinder rotation. J Comput Phys 2000;163:83–117.
[3] Chen W, Fu Y, Guo S, Jiang C. Fluid-solid coupling and dynamic response of vortex-induced vibration of slender ocean cylinders. Adv Mech 2017;47:25–91.
[4] Kumar RA, Sohn C-H, Gowda BH. Passive control of vortex-induced vibrations: an overview. Recent Pat Mech Eng 2008;1:1–11.
[5] Bearman P, Branković M. Experimental studies of passive control of vortex-induced vibration. Eur J Mech B Fluid 2004;23:9–15.
[6] Gao Y, Yang J, Xiong Y, Wang M, Peng G. Experimental investigation of the effects of the coverage of helical strakes on the vortex-induced vibration response of a flexible riser. Appl Ocean Res 2016;59:53–64.
[7] Gao Y, Fu S, Ren T, Xiong Y, Song L. VIV response of a long flexible riser fitted with strakes in uniform and linearly sheared currents. Appl Ocean Res 2015;52:102–14.
[8] Gao Y, Fu S, Ma L, Chen Y. Experimental investigation of the response performance of VIV on a flexible riser with helical strakes. Ships Offshore Struct 2016;11:113–28.
[9] Quen LK, Abu A, Kato N, Muhamad P, Sahekhaini A, Abdullah H. Investigation on the effectiveness of helical strakes in suppressing VIV of flexible riser. Appl Ocean Res 2014;44:82–91.
[10] Resvanis TL, Rao Z, Vandiver JK. Effects of strake coverage and marine growth on flexible cylinder VIV. International conference on offshore mechanics and arctic engineering. American Society of Mechanical Engineers; 2014. p. V002T08A77.
[11] How BVE, Ge SS, Choo YS. Active control of flexible marine risers. J Sound Vib 2009;320:758–76.
[12] Do KD, Pan J. Boundary control of transverse motion of marine risers with actuator dynamics. J Sound Vib 2008;318:768–91.
[13] Do KD, Pan J. Boundary control of three-dimensional inextensible marine risers. J Sound Vib 2009;327:299–321.
[14] Ge SS, He W, How BVE, Choo YS. Boundary control of a coupled nonlinear flexible marine riser. IEEE Trans Contr Syst Technol 2010;18:1080–91.
[15] Nguyen TL, Do KD, Pan J. Boundary control of two-dimensional marine risers with bending couplings. J Sound Vib 2013;332:3605–22.
[16] He W, Zhang S, Ge SS. Boundary control of a flexible riser with the application to marine installation. IEEE Trans Ind Electron 2013;60:5802–10.
[17] Zhang S, He X, Yang C. Vibration control of a flexible marine riser with joint angle constraint. Nonlinear Dynam 2017;87:617–32.
[18] Zhao Z, Liu Z, Li Z, Wang N, Yang J. Control design for a vibrating flexible marine riser system. J Franklin Inst 2017;354:8117–33.
[19] Shaharuddin NMR, Darus IZM. Active vibration control of marine riser. In: IEEE conference on control, systems & industrial informatics (ICCSII); 2012.
[20] Zhang W, Li D. Active control of axial dynamic response of deep-water risers with linear quadratic Gaussian controllers. Ocean Eng 2015;109:320–9.
[21] Yu J, Chen W. Active control of flexible riser vibration by boundary control based on LQR controller. Int Conf Offshore Mech Arctic Eng 2019;58806. V05AT04A049.
[22] Xue H, Tang W, Qu X. Prediction and analysis of fatigue damage due to cross-flow and in-line VIV for marine risers in non-uniform current. Ocean Eng 2014;83:52–62.
[23] Blevins RD. Flow-induced vibration. vnr; 1977.
[24] Faltinsen OM. Sea loads on ships and offshore structures. New York: Cambridge University Press; 1990.
[25] Vandiver JK, Li L. Shear7 V4. 4 program theoretical manual. Massachusetts Institute of Technology; 2005.
[26] Weaver W, Timoshenko S, Young D. Vibration problems in engineering. New York: Wiley; 1990.
[27] He J-B, Wang Q-G, Lee T-H. PI/PID controller tuning via LQR approach. Chem Eng Sci 2000;55:2429–39.
[28] Yu G-R, Hwang R-C. Optimal PID speed control of brush less DC motors using LQR approach. In: 2004 IEEE international conference on systems, man and cybernetics (IEEE cat No 04CH37583). IEEE; 2004. p. 473–8.
[29] Vandiver JK. SHEAR7 simulation, vol. 11. MIT; 2012. p. 10. http://web.mit.edu/shear7/shear7.html. MIT.
[30] Xu Y. Study on the frequency and time domain method in predicting vortex induced vibration of marine risers. Shanghai Jiao Tong University; 2014.